Nonvolatile electric field control of magnetism in bilayer CrI_3 on monolayer In_2Se_3

Hai-Xia Cheng,[1,2] Jun Zhou,[3] Cong Wang,[2] Wei Ji,[2,*] and Yan-Ning Zhang[1,†]

[1]*Institute of Fundamental and Frontier Sciences, University of Electronic Science and Technology of China, Chengdu 610054, China*

[2]*Department of Physics, Renmin University of China, Beijing 100872, China*

[3]*Institute of Materials Research and Engineering, 2 Fusionopolis Way, Singapore, 138634 Singapore*

(Received 8 April 2021; accepted 5 August 2021; published 26 August 2021)

Electrical control of magnetism is of great interest for low-energy-consumption spintronic applications. Here, via first-principles calculations, we propose a van der Waals (vdW) multiferroic heterostructure composed of a magnetic CrI_3 bilayer and a ferroelectric α-In_2Se_3 monolayer substrate. Interestingly, the interlayer magnetism of bilayer CrI_3 is switchable between the ferromagnetic and antiferromagnetic coupling by nonvolatile control of the ferroelectric polarization direction of α-In_2Se_3. The interlayer magnetic coupling of CrI_3 bilayer originates from the direct interaction of adjacent I atoms between CrI_3 monolayers, which can be tuned by the polarization of In_2Se_3, explaining the electrical control of interlayer magnetic phase transition. Our work demonstrates a multiferroelectric material platform by artificially stacking two dimensional vdW layers, providing an effective method for achieving nonvolatile electrical control of atomic-thin vdW ferromagnets.

DOI: 10.1103/PhysRevB.104.064443

I. INTRODUCTION

Magnetoelectric multiferroic materials exhibit coupled magnetic ordering and electric polarization, which allows electrical control of magnetism, promising for next-generation devices with low-dissipation electric writing and fast magnetic reading functions [1–3]. In accompany with continuous miniaturization and increasing integration of spintronic devices, two dimensional (2D) multiferroic materials have become one of the hottest research topics in the condensed matter physics and materials science [3]. However, single-phase 2D multiferroic materials are rare because of the inherent mutual exclusion between magnetism and electrical polarization. While magnetism usually results from partially filled orbitals, ferroelectricity arises from off-center cations requiring completely empty or occupied orbitals [4].

van der Waals (vdW) heterostructures have been successfully synthesized [5–8] and offer an exciting platform to integrate 2D materials with various properties, generating opportunities to explore new possibilities such as 2D multiferroics. Due to the atomically clean interface, a van der Waals heterostructure integration of a 2D magnet and a 2D ferroelectric material may preserve their original magnetic and electrical orders, providing a scalable pathway to obtain 2D multiferroics. With the coexistence of these orders, controllably tuning one order could manipulate the other, realizing multiferroic functions through regulating interlayer coupling in certain layered materials with specified stacking orders.

2D magnets such as CrI_3 [9], $CrGeTe_3$ [10], VSe_2 [11] as well as Fe_3GeTe_2 [12] and 2D ferroelectric (FE) layers, e.g., 1T'-WTe_2 [13], α-In_2Se_3 [14–16], and SnTe [17], have been recently synthesized in experiments. Among them, bilayer (BL) CrI_3 is of particular interest because of its intralayer ferromagnetism and manipulatable interlayer magnetism between antiferromagnetic (AFM) and ferromagnetic (FM) coupling [18,19]. Such manipulation in a volatile manner of BL-CrI_3 has been demonstrated experimentally by electric gating [20,21], high pressure [22,23], or a reasonably large magnetic field [24]. This switchable interlayer magnetism of BL-CrI_3 through electrical field implies it to be a potential component for constructing a multiferroic van der Waals heterostructure, in which the magnetism might be tuned by a nonvolatile electrical polarization field.

Two-dimensional α-In_2Se_3 is an ideal candidate to introduce the ferroelectric order to multiferroic van der Waals heterostructures. The middle Se atoms are off center, which breaks the centrosymmetry of In_2Se_3 and generates a net out-of-plane electric polarization at room temperature [14,16]. The obtained small polarization barrier of 66 meV [25] corresponds to an experimental coercive electric field of around 2 mV/Å [16]. The ferroelectric polarization of In_2Se_3 persists on different substrates [16,25], and is robust against the depolarization electric field in ultrathin α-In_2Se_3 as the intrinsic interlocking of in-plane and out-of-plane electric dipoles stemming from its lattice structure [14,15]. Moreover, in In_2Se_3-based heterostructures it has recently been theoretically shown that switching the direction of electrical polarization in α-In_2Se_3 could affect the electronic band gaps [26], magnetic couplings [27], and the magnetization direction [28] of its adlayers. These pioneering studies might imply that α-In_2Se_3 can also provide a nonvolatile route to switch the interlayer magnetism of BL-CrI_3 but does not change the semiconducting nature of the heterostructure, the latter of which is essential for a reversible manipulation.

Here, we propose that the formation of a multiferroic heterostructure between high temperature (HT)-BL-CrI_3 and

*Corresponding author: wji@ruc.edu.cn

†Corresponding author: yanningz@uestc.edu.cn

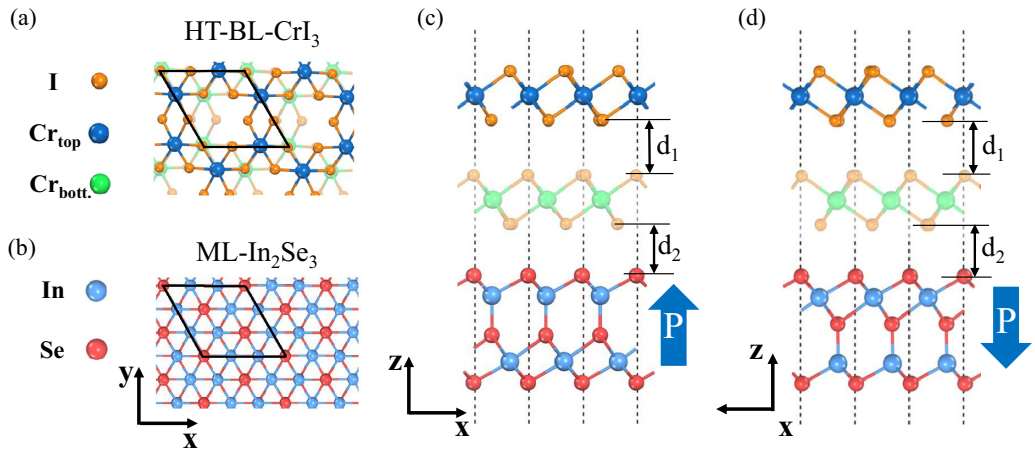

FIG. 1. Top view of (a) HT-BL-1 × 1 CrI_3 and (b) $\sqrt{3} \times \sqrt{3}$ In_2Se_3 monolayer. Side views of HT-BL-CrI_3/In_2Se_3 heterostructures with the In_2Se_3 ferroelectric dipole moment directed (c) upward and (d) downward, respectively. Black rhombuses in (a) and (b) refer to the HT-BL-CrI_3 unit cell and $\sqrt{3} \times \sqrt{3}$ In_2Se_3 supercell.

α-In_2Se_3 monolayer is possible with a small lattice mismatch. Interestingly, we show that flipping the polarization direction of the α-In_2Se_3 layer switches the interlayer magnetism of HT-BL-CrI_3. Such a switch is found to originate from the ferroelectric polarization dependent hopping strengths of the different channels [19] between interfacial I atoms from each CrI_3 layer. The nonvolatile electrical control of magnetism is robust even under the enlarged interface distance between CrI_3 and In_2Se_3 because it is governed by a mechanism in which the electric field of the nonvolatile FE material plays a dominant role.

II. METHODOLOGY

Spin-polarized density functional theory (DFT) calculations were performed using the projector augmented wave [29,30] method as implemented in the Vienna *ab initio* simulation package [31,32]. The optB86b-vdW exchange correlation functional was chosen for the van der Waals corrections [33–35]. The Perdew-Burke-Ernzerhof [36] functional was adopted to conduct total energy, magnetism, and electronic structure calculations. An on-site Coulomb interaction with $U = 3.9$ eV and $J = 0.9$ eV was considered for the Cr−3d orbitals [19]. The kinetic energy cutoff of 500 eV for the plane-wave basis set was found to be sufficient for the CrI_3/α-In_2Se_3 heterostructures. The Brillouin zone was sampled using a uniform Γ-centered 7 × 7 × 1 Monkhorst-pack k mesh for structural relaxations and 11 × 11 × 1 for electronic structures and magnetism calculations. Spin-orbit coupling (SOC) was considered in total energy and electronic structure calculations.

The CrI_3/In_2Se_3 heterostructure was modeled using a 1 × 1 CrI_3 bilayer with AFM coupling in which stacking order is the high temperature (HT) phase of its bulk crystal [18,19] [Fig. 1(a)] and a $\sqrt{3} \times \sqrt{3}$ α-In_2Se_3 monolayer (ML) [Fig. 1(b)] with a lattice mismatch of less than 2%, denoted as HT-BL-CrI_3/In_2Se_3. A vacuum layer of 20 Å was used to eliminate interactions between periodic images. Lattice constants and atomic positions were fully relaxed until the residual force on each atom was less than 0.01 eV/Å. DFT calculated lattice parameters of ground state (AFM) 1 × 1 HT-BL-CrI_3 and 1 × 1 α-In_2Se_3 are $a = b = 6.900$ Å and $a = b = 4.074$ Å, respectively, and the energy of HT-BL-CrI_3 in the AFM state is 0.48 meV/Cr lower than that of the FM state. These results are in good agreement with previous theoretical values [18,19,25], indicating the accuracy of the calculation method and the parameters we adopted. The magnetocrystalline anisotropy energy (MAE) was extracted by calculating the energy difference between the cases in which all magnetic moments of Cr were oriented along the a and c lattice vectors, respectively. A dipole correction perpendicular to the heterostructure was applied to eliminate spurious dipole-dipole interaction between periodic images.

III. RESULTS AND DISCUSSIONS

A. Structural properties of HT-BL-CrI_3/In_2Se_3 heterostructure

Three possible vertical stackings including hollow, top, bridge configurations are considered for HT-BL-CrI_3/In_2Se_3 heterostructure as shown in Fig. S1 of the Supplemental Material [37]. Among them, the hollow stacking [Figs. 1(c) and 1(d)] in which interfacial I atoms sit at the hollow sites of interfacial Se hexagons is found to be energetically lower than that of the top (bridge) one by 6.914 (1.405) and 6.905 (1.125) meV/atom for upward (P-up) and downward (P-down) polarized In_2Se_3, respectively. Thus, HT-BL-CrI_3/In_2Se_3 refers to the hollow configuration in the following unless stated otherwise. Table S1 [37] lists the structural information of the hollow stacking HT-BL-CrI_3/In_2Se_3 heterostructure with opposite polarization directions, i.e., the P-up and P-down states. The interlayer I-I distance (d_1 as denoted in Fig. 1) in the P-up state (3.496 Å) is 0.015 Å larger than that of the P-down state (3.481 Å) for the AFM configuration, but almost equivalent to the pristine HT-BL-CrI_3's (3.495 Å). Moreover, the equilibrium I-Se interface distance (d_2 as denoted in Fig. 1) reduces from 3.321 to 3.296 Å as the polarization direction of In_2Se_3 flips from upward to downward, increasing correspondingly the interface strength between HT-BL-CrI_3 and In_2Se_3. The smaller I-I and I-Se interlayer distances in the P-down state may modulate the charge distribution and

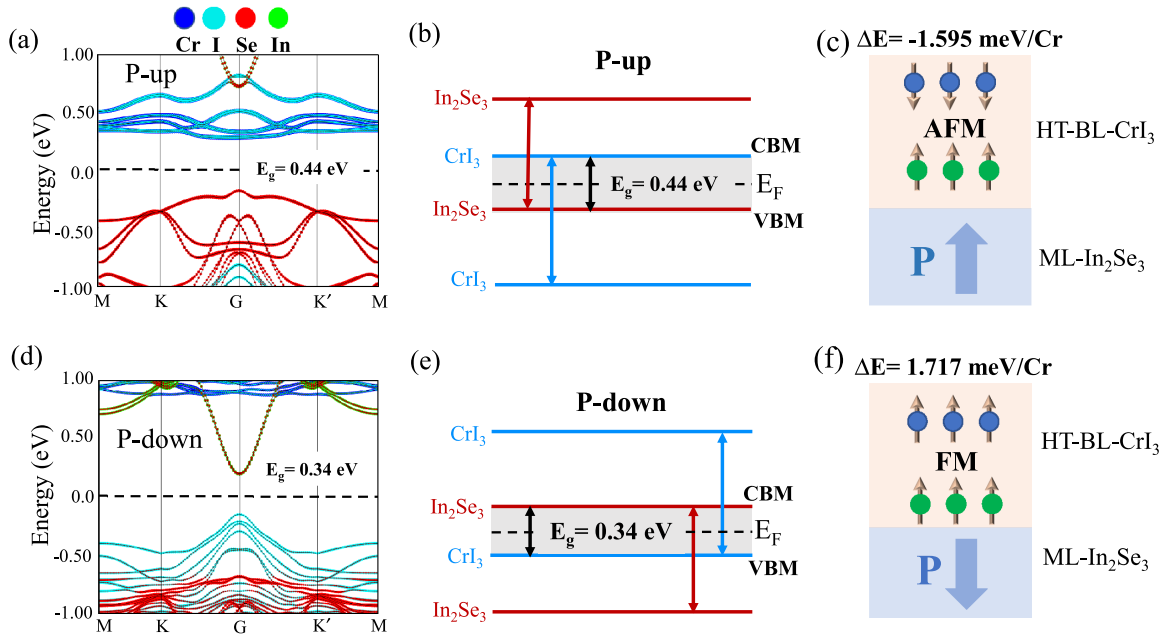

FIG. 2. Atomic decomposed band structures with SOC, the VBM and CBM schematic diagram of HT-BL-CrI_3/In_2Se_3 heterostructures (a),(b) for P-up and (d),(e) for P-down of In_2Se_3, respectively. The induced interlayer magnetic coupling between Cr atom layers switches from (b) AFM to (d) FM. The blue (green) solid circles refer to the Cr atoms at the top (bottom) layer, light brown arrows refer to the spin direction of Cr atoms, and large blue arrows stand for the ferroelectric polarization direction of In_2Se_3. The energy difference is defined by $\Delta E = E_{\mathrm{AFM}} - E_{\mathrm{FM}}$. A negative value indicates that the HT-BL-CrI_3 prefers an interlayer antiferromagnetic coupling for an upward polarization of In_2Se_3 and vice versa.

thus influence the interlayer magnetic coupling of HT-BL-CrI_3. Furthermore, the thickness of the two CrI_3 monolayers in HT-BL-CrI_3 adlayer is no longer the same (Fig. S2 [37]), illustrating that its spatial inversion symmetry is broken by the In_2Se_3 substrate.

B. Electronic structure and magnetoelectric coupling properties

Figures 2(a) and 2(d) show the band structures of HT-BL-CrI_3/In_2Se_3 at P-up and P-down configurations, respectively. Both configurations offer direct band gaps at the Γ point of 0.44 and 0.34 eV, respectively. In the P-up state, the valence band maximum (VBM) and conduction band minimum (CBM) of the heterostructure are mainly composed of the In_2Se_3 and CrI_3, respectively [see Figs. 2(a) and 2(b)]. When switching the polarization direction of In_2Se_3 to downward, the total dipole moment of the heterostructure is also reversed relative to the P-up configuration since the intrinsic electric polarization of In_2Se_3 is dominant in the heterostructure. The reversed polarization causes a switched determination of VBM (CrI_3) and CBM (In_2Se_3) as well as a reduced band gap of 0.34 eV as shown in Figs. 2(d) and 2(e).

The HT-BL-CrI_3/In_2Se_3 heterostructure contains an intrinsically ferroelectric In_2Se_3 layer and a magnetic HT CrI_3 bilayer. We may expect a magnetoelectric coupling effect in the HT-BL-CrI_3/In_2Se_3 heterostructure manipulated by electrically switching the In_2Se_3 polarization. The overall out-of-plane dipole moment of the heterostructure is 0.10 (−0.07) e Å/In_2Se_3 in the P-up (P-down) state, which is contributed by the intrinsic moment in In_2Se_3 ($D_{\mathrm{intrinsic}} = 0.09$ e Å/In_2Se [25]) and the interface induced dipole moment at the CrI_3/In_2Se_3 interface ($D_{\mathrm{interface}} \approx$ 0.01 and 0.02 e Å/In_2Se_3 in the P-up and -down state, respectively). In the P-up state, the interfacial moment is oriented in the same direction as the intrinsic moment (see Fig. S3 [37]), reinforcing the electrical field applied on the CrI_3 bilayer. Conversely, the electrical field is negative in the P-down state, and it is slightly weakened since the dominant intrinsic moment in In_2Se_3 is antiparallel to the interfacial one (see Fig. S3 [37]).

In each of the two polarization states, we compared the total energies of the heterostructures for the CrI_3 bilayer in the interlayer AFM and FM configurations, respectively. In the P-up state, the interlayer AFM configuration of the CrI_3 bilayer is ∼1.595 meV/Cr more favored than the interlayer FM configuration, as shown in Fig. 2(c). Excitingly, the interlayer FM configuration becomes the ground state of the CrI_3 bilayer in the P-down state by 1.717 meV/Cr lower than the interlayer AFM, as shown in Fig. 2(f). This trend doesn't change by applying different DFT-vdW functionals, and ΔE by the hybrid functional (HSE), −1.386 meV/Cr (1.771 meV/Cr) for P-up (P-down) polarization of In_2Se_3, is close to the values predicted by PBE, as shown in Table S2 [37]. The ΔE also change negligibly by flipping the spin polarization of the two CrI_3 layers simultaneously since the ML-In_2Se_3 is not magnetized by neighboring CrI_3. The magnetic moment of each Cr atom in the heterostructure (3.01 μ_B) is almost the same as that in the pristine HT-BL-CrI_3 (3.00 μ_B). Furthermore, HT-BL-CrI_3 keeps the out-of-plane easy magnetization axis (along c axis) in the heterostructure but is slightly reduced by ∼0.03 meV/Cr (P-up) and 0.01 meV/Cr (P-down) compared to the pristine value of 0.236 meV/Cr (Table S3 [37]). In

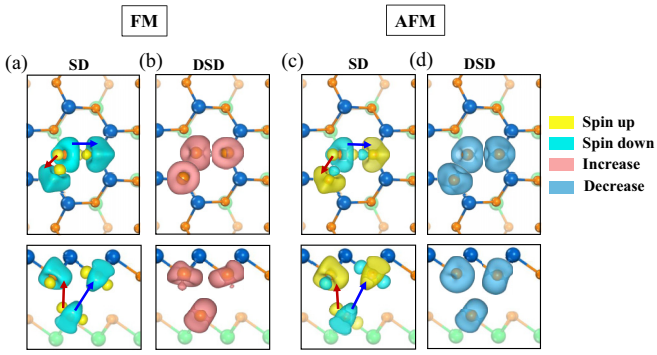

FIG. 3. (a),(c) Spin density (SD) of HT-BL-CrI_3/In_2Se_3 and (b),(d) differential spin density (DSD) between P-down and P-up HT-BL-CrI_3/In_2Se_3 in FM configuration (left side) and AFM configuration (right side). The yellow and cyan isosurface in (a) and (c) refer to spin-up and -down density, respectively. The increase and decrease of spin density (absolute value) are shown with red and blue isosurface in (b) and (d), respectively. The isosurface value of SD and DSD is 6×10^{-4} and 2×10^{-6} e/bohr^3, respectively. Red and blue arrows stand for the $p_{x/y} - p_z$ and $p_{x/y} - p_{x/y}$ orbital hopping between interlayer I atoms.

a word, switching the polarization direction of In_2Se_3 from up (positive) to down (negative) changes the magnetic ground state of HT-BL-CrI_3 from the interlayer AFM to FM ordering while it keeps the size and orientation of easy magnetic axis. The switching of the polarization in In_2Se_3 monolayer has been observed experimentally in an FE-based device [16], and thus the screening effects from the substrate should be expected to be marginal [38,39].

C. Mechanism of electrically controlled interlayer magnetic coupling

The interlayer magnetic coupling of HT-BL-CrI_3 has been shown to be determined by the direct interaction of the adjacent I atoms from each CrI_3 monolayer [19]. To understand the underlying mechanism of the interlayer magnetic phase transition of HT-BL-CrI_3 by reversing the electrical polarization of In_2Se_3 as shown above, we analyze the spin density (SD) and differential spin density (DSD) between P-down and P-up states of the interlayer I atoms for HT-BL-CrI_3 in FM [Figs. 3(a) and 3(b)] and AFM [Figs. 3(c) and 3(d)] configuration, respectively. We define the orbitals distributed along the directions of Cr-I bonds as the I$-p_{x/y}$ [cyan isosurface in Fig. 3(a)], and the orbital in their perpendicular direction as the I$-p_z$ [yellow isosurface in Fig. 3(a)] [19]. As shown in Figs. 3(a) and 3(c), the $p_{x/y}$ orbital has the opposite spin component to p_z within one I atom. And there are also couplings between the p orbitals of adjacent I atoms in the different CrI_3 layers, that is, $p_{x/y} - p_z$ and $p_{x/y} - p_{x/y}$ as indicated by the red and blue arrows in Fig. 3, respectively.

As the DSD plotted in Fig. 3(b) for the FM configuration, reversing the electric polarization direction from up to down primarily increases the charge density mostly in the spin-down component of the I$-p_{x/y}$ orbitals [see Fig. 3(a)]. The enlarged spin density thus exclusively enhances the FM hopping between the two neighboring I atomic layers. For the AFM configuration, the majority spins ($p_{x/y}$) are oppositely oriented for the two adjacent I atomic layers, as shown in Fig. 3(c). The flipping of the polarization direction from up to down reduces the spin density of either spin-up or -down component for the interlayer I$-p_{x/y}$ orbitals [see Fig. 3(d)]. Therefore, the interlayer AFM hopping is weakened because of the decreased spin-up and -down densities of the interlayer I$-p_{x/y}$ orbitals. Table S4 [37] shows the enlarged and diminished magnetic moments of the interfacial I atoms in the interlayer FM and AFM configurations, respectively, qualitatively supporting the change of spin density of the interlayer I$-p_{x/y}$ orbital.

Such a change of spin density of interlayer I$-p_{x/y}$ orbitals could be understood based on the electrical polarization dependent band alignment between CrI_3 and In_2Se_3 (Fig. 4) and differential charge density (DCD) at the I-I interface (Fig. S4 [37]). The HT-BL-CrI_3 is symmetric and both sides have the same electrostatic potential [Fig. 4(a)], while In_2Se_3 has an asymmetric structure thus its electrostatic potential is different for two sides [Fig. 4(b)]. As HT-BL-CrI_3 contacts with oppositely polarized In_2Se_3, we can see different band alignments shown in Fig. 4(c). For the P-up state, the energy difference between the VBM of In_2Se_3 and the CBM of HT-BL-CrI_3 is small, causing obvious charge redistribution between In_2Se_3 and CrI_3 interface [Fig. S4(a) [37]], as well as abundant charge accumulation at the I-I interface in CrI_3 bilayer [Fig. S4(c) [37]]. As a comparison, the larger energy difference between the VBM of P-down In_2Se_3 and the CBM of HT-BL-CrI_3 induces charge transfer from the I layer in the I-Se interface to the outmost I layer [Fig. S4(b) [37]] and relatively less charge accumulation in between two CrI_3 layers [Fig. S4(d) [37]]. The HSE06 calculated band alignment in Fig. S5 [37] also indicates the charge redistribution at I-Se and I-I interfaces for different electric polarization states of In_2Se_3 but with a type II band alignment between P-up In_2Se_3 and CrI_3. Furthermore, the electric field regulates the interlayer potential energy (Fig. S6 [37]) between CrI_3 bilayer, which also changes the interlayer exchange coupling. Overall, flipping the polarization of In_2Se_3 from upward to downward induces an opposite electric field on HT-BL-CrI_3 in the heterostructure and modulates the charge distribution at the I-I interface space of HT-BL-CrI_3, making the FM coupling in the Cr-I…I-Cr direct interaction more preferred than the AFM hopping of HT-BL-CrI_3.

D. Effects of different I-Se interface distances and external electric field

The discussion above demonstrated that the interlayer magnetic ordering of HT-BL-CrI_3 is dependent on the polarization of In_2Se_3, which also changes the interfacial distance between CrI_3 and In_2Se_3. In this section, we further study the effects of different interface I-Se vertical distances (d_2) on the magnetic properties of HT-BL-CrI_3 with both the P-up and P-down state of In_2Se_3. As shown in Fig. 5(a), the increased d_2 from ~2.8 Å to ~3.3 Å slightly increases the MAE from 0.76 to 0.83 meV for the P-up state and converges to 0.88 meV at ~5.0 Å. The d_2 dependence of MAE in the P-down state shares the same trend as that of P-up. Overall, the easy magnetization axis keeps along the out-of-plane direction regardless of the interfacial distances studied in this work.

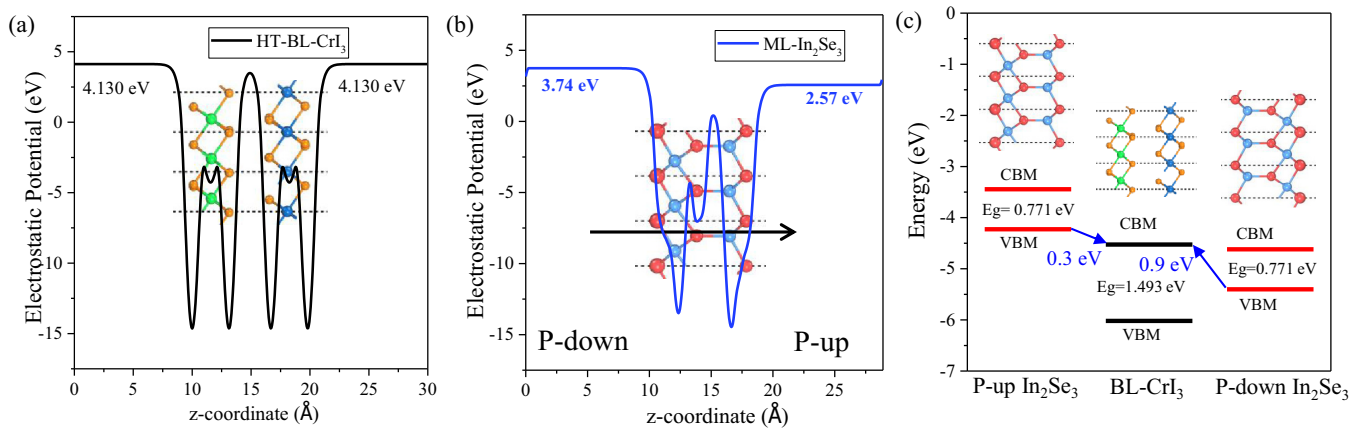

FIG. 4. The electrostatic potential of (a) HT-BL-CrI_3 and (b) ML-In_2Se_3. (c) PBE + U calculated band alignments between HT-BL-CrI_3 and ML-In_2Se_3 with different polarization directions. All the energy levels are shifted relative to the vacuum level of HT-BL-CrI_3.

As shown in Fig. 5(b), the interlayer magnetic coupling strength is enhanced by several folds at a small d_2 of ∼2.8 Å compared with the case in the equilibrium distance. This can be understood by the d_2-dependent interface-induced dipole moments ($D_{\text{interface}}$), which is substantially reinforced as the In_2Se_3 and HT-BL-CrI_3 layers approach each other. The larger $D_{\text{interface}}$ leads to an increased (decreased) total dipole moment of the heterostructure in the P-up (down) state (Fig. S7 [37]) because their dipole moment orientation between $D_{\text{intrinsic}}$ and $D_{\text{interface}}$ is parallel (antiparallel) (Fig. S3 [37]). As the d_2 increases to about 5.0 Å, the AFM coupling strength for the P-up state approaches the magnitude of the pristine HT-BL-CrI_3 (−0.48 meV/Cr), but the FM coupling strength of the P-down state is converged to 1.25 meV/Cr. This difference mainly arises from the varied equilibrium I-I interlayer distance (d_1) between the P-down and P-up states. In terms of the P-down state, distance d_1 of the AFM configuration is 0.018 Å smaller than that of the FM configuration, as shown in Table S1 [37]. They are, however, nearly equivalent in the P-up state.

Herein, we apply an external out-of-plane electric field by adding a dipole in the vacuum region [40,41] to the heterostructure that their states are FM P-down and AFM P-up, respectively, to examine the stabilities of these states. As shown in Fig. 5(c), a negative electric field (along the negative direction of the c axis) enlarges the energy difference between the two states and further stabilizes the FM P-down state. In contrast, the AFM P-up state is more stable in a positive electric field and becomes the ground state as the electric field is larger than ∼0.02 V/Å. It is interesting to note that a negative or a small positive (<0.02 V/Å) external electric field will promote the electrical polarization flipping induced interlayer AFM to FM transition of HT-BL-CrI_3. Thus, the HT-BL-CrI_3/In_2Se_3 heterostructure is a promising multiferroic material with the potential for multistate storage, appealing to realize a controllable magnetic reading and electric writing function. We also studied the electronic and magnetic properties of BL-CrI_3/In_2Se_3 heterostructures with low temperature (LT) stacking order of bulk CrI_3, denoted as LT-BL-CrI_3/In_2Se_3, as shown in Fig. S8 and Tables S5 and S6 [37], where the electrical-field-controlled magnetism transition was not observed.

IV. CONCLUSIONS

In summary, we theoretically proposed a heterostructure comprised of HT-BL-CrI_3 and ML-In_2Se_3. The built-in

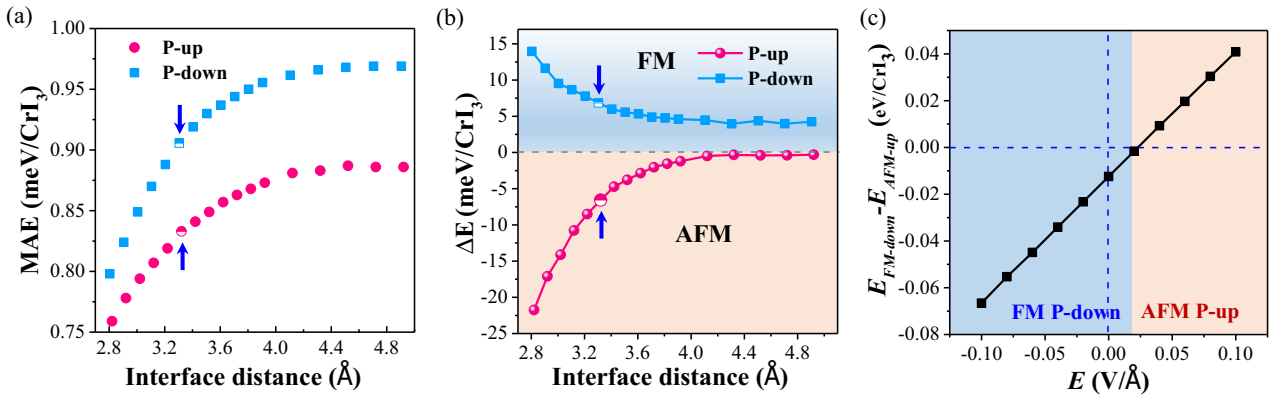

FIG. 5. Evolution of (a) magnetocrystalline anisotropy energy and (b) energy difference between AFM and FM configurations of HT-BL-CrI_3/In_2Se_3 with P-up and P-down of In_2Se_3 under various I-Se vertical interface distances. The blue arrows denote the equilibrium interfacial spacing position. (c) The energy difference between FM ground state of P-down HT-BL-CrI_3/In_2Se_3 and AFM ground state of P-up one as a function of the external electric field. The blue and orange region stands for the FM and AFM coupling, respectively.

electric field in the heterostructure is contributed by the intrinsic polarization of α-In_2Se_3 and a weaker interface-induced dipole moment at the CrI_3/In_2Se_3 interface. The magnitude of the total electric field is larger in the *P*-up state than in the *P*-down state as the intrinsic ferroelectric field is parallel with the interface-induced field in the former case while opposite in the latter. The negative internal electrical field in the *P*-down state enhances the spin polarization of interlayer I atoms and strengthens their direct interlayer FM interaction, thus promoting an interlayer FM coupling of HT-BL-CrI_3, in contrast with the interlayer AFM coupling of HT-BL-CrI_3. These results illustrate an effective way of manipulating interlayer magnetic coupling of 2D vdW magnetic materials by nonvolatile electrical control. More experimental and theoretical studies are expected in this respect to accelerate their practical applications in nonvolatile high-density data storage devices.

ACKNOWLEDGMENTS

This research is supported by the National Natural Science Foundation of China (Grant No. 11874005). Calculations were performed at the Physics Lab of High-Performance Computing of the Renmin University of China.

[1] M. Fiebig, T. Lottermoser, D. Meier, and M. Trassin, Nat. Rev. Mater. **1**, 16046 (2016).
[2] T. Hu and E. Kan, WIREs Comput. Mol. Sci. **9**, e1409 (2019).
[3] T. Kimura, T. Goto, H. Shintani, K. Ishizaka, T. Arima, and Y. Tokura, Nature (London) **426**, 55 (2003).
[4] N. A. Hill, J. Phys. Chem. B **104**, 6694 (2000).
[5] J. Li, X. Yang, Y. Liu, B. Huang, R. Wu, Z. Zhang, B. Zhao, H. Ma, W. Dang, Z. Wei, K. Wang, Z. Lin, X. Yan, M. Sun, B. Li, X. Pan, J. Luo, G. Zhang, Y. Liu, Y. Huang, X. Duan, and X. Duan, Nature (London) **579**, 368 (2020).
[6] A. K. Geim and I. V. Grigorieva, Nature (London) **499**, 419 (2013).
[7] Y. Liu, N. O. Weiss, X. Duan, H.-C. Cheng, Y. Huang, and X. Duan, Nat. Rev. Mater. **1**, 16042 (2016).
[8] K. S. Novoselov, A. Mishchenko, A. Carvalho, and A. H. Castro Neto, Science **353**, aac9439 (2016).
[9] B. Huang, G. Clark, E. Navarro-Moratalla, D. R. Klein, R. Cheng, K. L. Seyler, D. Zhong, E. Schmidgall, M. A. McGuire, D. H. Cobden, W. Yao, D. Xiao, P. Jarillo-Herrero, and X. Xu, Nature (London) **546**, 270 (2017).
[10] C. Gong, L. Li, Z. Li, H. Ji, A. Stern, Y. Xia, T. Cao, W. Bao, C. Wang, Y. Wang, Z. Q. Qiu, R. J. Cava, S. G. Louie, J. Xia, and X. Zhang, Nature (London) **546**, 265 (2017).
[11] M. Bonilla, S. Kolekar, Y. Ma, H. C. Diaz, V. Kalappattil, R. Das, T. Eggers, H. R. Gutierrez, M.-H. Phan, and M. Batzill, Nat. Nanotechnol. **13**, 289 (2018).
[12] Z. Fei, B. Huang, P. Malinowski, W. Wang, T. Song, J. Sanchez, W. Yao, D. Xiao, X. Zhu, A. F. May, W. Wu, D. H. Cobden, J.-H. Chu, and X. Xu, Nat. Mater. **17**, 778 (2018).
[13] Z. Fei, W. Zhao, T. A. Palomaki, B. Sun, M. K. Miller, Z. Zhao, J. Yan, X. Xu, and D. H. Cobden, Nature (London) **560**, 336 (2018).
[14] C. Cui, W.-J. Hu, X. Yan, C. Addiego, W. Gao, Y. Wang, Z. Wang, L. Li, Y. Cheng, P. Li, X. Zhang, H. N. Alshareef, T. Wu, W. Zhu, X. Pan, and L.-J. Li, Nano Lett. **18**, 1253 (2018).
[15] J. Xiao, H. Zhu, Y. Wang, W. Feng, Y. Hu, A. Dasgupta, Y. Han, Y. Wang, D. A. Muller, L. W. Martin, P. A. Hu, and X. Zhang, Phys. Rev. Lett. **120**, 227601 (2018).
[16] F. Xue, W. Hu, K.-C. Lee, L.-S. Lu, J. Zhang, H.-L. Tang, A. Han, W.-T. Hsu, S. Tu, W.-H. Chang, C.-H. Lien, J.-H. He, Z. Zhang, L.-J. Li, and X. Zhang, Adv. Funct. Mater. **28**, 1803738 (2018).
[17] K. Chang, J. Liu, H. Lin, N. Wang, K. Zhao, A. Zhang, F. Jin, Y. Zhong, X. Hu, W. Duan, Q. Zhang, L. Fu, Q.-K. Xue, X. Chen, and S.-H. Ji, Science **353**, 274 (2016).
[18] N. Sivadas, S. Okamoto, X. Xu, C. J. Fennie, and D. Xiao, Nano Lett. **18**, 7658 (2018).
[19] P. Jiang, C. Wang, D. Chen, Z. Zhong, Z. Yuan, Z.-Y. Lu, and W. Ji, Phys. Rev. B **99**, 144401 (2019).
[20] D. R. Klein, D. MacNeill, J. L. Lado, D. Soriano, E. Navarro-Moratalla, K. Watanabe, T. Taniguchi, S. Manni, P. Canfield, J. Fernández-Rossier, and P. Jarillo-Herrero, Science **360**, 1218 (2018).
[21] T. Song, X. Cai, M. W.-Y. Tu, X. Zhang, B. Huang, N. P. Wilson, K. L. Seyler, L. Zhu, T. Taniguchi, K. Watanabe, M. A. McGuire, D. H. Cobden, D. Xiao, W. Yao, and X. Xu, Science **360**, 1214 (2018).
[22] T. Li, S. Jiang, N. Sivadas, Z. Wang, Y. Xu, D. Weber, J. E. Goldberger, K. Watanabe, T. Taniguchi, C. J. Fennie, K. Fai Mak, and J. Shan, Nat. Mater. **18**, 1303 (2019).
[23] F. Subhan, I. Khan, and J. Hong, J. Phys.: Condens. Matter **31**, 355001 (2019).
[24] Z. Wang, I. Gutiérrez-Lezama, N. Ubrig, M. Kroner, M. Gibertini, T. Taniguchi, K. Watanabe, A. Imamoğlu, E. Giannini, and A. F. Morpurgo, Nat. Commun. **9**, 2516 (2018).
[25] W. Ding, J. Zhu, Z. Wang, Y. Gao, D. Xiao, Y. Gu, Z. Zhang, and W. Zhu, Nat. Commun. **8**, 14956 (2017).
[26] F. Xue, Z. Wang, Y. Hou, L. Gu, and R. Wu, Phys. Rev. B **101**, 184426 (2020).
[27] W. Sun, W. Wang, D. Chen, Z. Cheng, and Y. Wang, Nanoscale **11**, 9931 (2019).
[28] C. Gong, E. M. Kim, Y. Wang, G. Lee, and X. Zhang, Nat. Commun. **10**, 2657 (2019).
[29] G. Kresse and D. Joubert, Phys. Rev. B **59**, 1758 (1999).
[30] P. E. Blöchl, Phys. Rev. B **50**, 17953 (1994).
[31] G. Kresse and J. Furthmüller, Phys. Rev. B **54**, 11169 (1996).
[32] G. Kresse and J. Furthmüller, Comput. Mater. Sci. **6**, 15 (1996).
[33] J. Klimeš, D. R. Bowler, and A. Michaelides, J. Phys.: Condens. Matter **22**, 022201 (2009).
[34] M. Dion, H. Rydberg, E. Schröder, D. C. Langreth, and B. I. Lundqvist, Phys. Rev. Lett. **92**, 246401 (2004).
[35] J. Klimeš, D. R. Bowler, and A. Michaelides, Phys. Rev. B **83**, 195131 (2011).
[36] J. P. Perdew, K. Burke, and M. Ernzerhof, Phys. Rev. Lett. **80**, 891 (1998).

[37] See Supplemental Material at http://link.aps.org/supplemental/10.1103/PhysRevB.104.064443 for more simulation results on the structural, electronic, and magnetic properties of HT-BL-CrI_3/In_2Se_3 and LT-BL-CrI_3/In_2Se_3 heterostructures.

[38] A. Ambrosetti and P. L. Silvestrelli, J. Phys. Chem. Lett. **10**, 2044 (2019).

[39] A. Ambrosetti and P. L. Silvestrelli, Carbon **139**, 486 (2018).

[40] P. J. Feibelman, Phys. Rev. B **64**, 125403 (2001).

[41] J. Neugebauer and M. Scheffler, Phys. Rev. B **46**, 16067 (1992).